ELSEVIER

Contents lists available at ScienceDirect

# Earth and Planetary Science Letters

www.elsevier.com/locate/epsl



# Triggered crustal earthquake swarm across subduction segment boundary after the 2016 Pedernales, Ecuador megathrust earthquake



Mariah C. Hoskins <sup>a,\*</sup>, Anne Meltzer <sup>a</sup>, Yvonne Font <sup>b</sup>, Hans Agurto-Detzel <sup>b</sup>, Sandro Vaca <sup>c</sup>, Frederique Rolandone <sup>d</sup>, Jean-Mathieu Nocquet <sup>b</sup>, Lillian Soto-Cordero <sup>a</sup>, Joshua C. Stachnik <sup>a</sup>, Susan Beck <sup>e</sup>, Colton Lynner <sup>e,f</sup>, Mario Ruiz <sup>c</sup>, Alexandra Alvarado <sup>c</sup>, Stephen Hernandez <sup>c</sup>, Philippe Charvis <sup>b</sup>, Marc Regnier <sup>b</sup>, Sergio Leon-Rios <sup>g</sup>, Andreas Rietbrock <sup>g</sup>

- <sup>a</sup> Department of Earth and Environmental Sciences, Lehigh University, 9A STEPS Bldg. 1 W. Packer Ave., Bethlehem, PA, 18015, USA
- <sup>b</sup> Université Côte d'Azur IRD, CRNS, Observatoire de la Côte d'Azur, Géoazur, UMR 7329, Valbonne, France
- <sup>c</sup> Instituto Geofísico at the Escuela Politécnica Nacional, Av. Ladrón de Guevara E11-253, Quito 170525, Ecuador
- <sup>d</sup> Sorbonne Université, CNRS-INSU, Institut des Sciences de la Terre Paris, ISTeP, UMR 7193, Paris, France
- e Department of Geosciences, University of Arizona, 1040 E. 4th St., Tucson, AZ, 85721, USA
- f Department of Earth Sciences, University of Delaware, 255 Academy St., Newark, DE, 19716, USA
- g Geophysical Institute (GPI), Karlsruhe Institute of Technology, 76187 Karlsruhe, Germany

#### ARTICLE INFO

# Article history: Received 22 November 2019 Received in revised form 25 September 2020 Available online 9 October 2020 Editor: J.P. Avouac

Keywords: triggered seismicity upper plate deformation postseismic deformation megathrust rupture earthquake swarm aftershocks

#### ABSTRACT

Megathrust ruptures and the ensuing postseismic deformation cause stress changes that may induce seismicity on upper plate crustal faults far from the coseismic rupture area. In this study, we analyze seismic swarms that occurred in the north Ecuador area of Esmeraldas, beginning two months after the 2016  $M_{\rm w}$  7.8 Pedernales, Ecuador megathrust earthquake. The Esmeraldas region is 70 km from the Pedernales rupture area in a separate segment of the subduction zone. We characterize the Esmeraldas sequence, relocating the events using manual arrival time picks and a local a-priori 3D velocity model. The earthquake locations from the Esmeraldas sequence outline an upper plate fault or shear zone. The sequence contains one major swarm and several smaller swarms. Moment tensor solutions of several events include normal and strike-slip motion and non-double-couple components. During the main swarm, earthquake hypocenters increase in distance from the first event over time, at a rate of a few hundred meters per day, consistent with fluid diffusion. Events with similar waveforms occur within the sequence, and a transient is seen in time series of nearby GPS stations concurrent with the seismicity. The events with similar waveforms and the transient in GPS time series suggest that slow aseismic slip took place along a crustal normal fault during the sequence. Coulomb stress calculations show a positive Coulomb stress change in the Esmeraldas region, consistent with seismicity being triggered by the Pedernales mainshock and large aftershocks. The characteristics of the seismicity indicate that postseismic deformation involving fluid flow and slow slip activated upper plate faults in the Esmeraldas area. These findings suggest the need for further investigation into the seismic hazard potential of shallow upper plate faults and the potential for megathrust earthquakes to trigger slow-slip and shallow seismicity across separate segments of subduction zones.

© 2020 The Authors. Published by Elsevier B.V. This is an open access article under the CC BY-NC-ND license (http://creativecommons.org/licenses/by-nc-nd/4.0/).

## 1. Introduction

Seismicity triggered in the shallow upper crust by megathrust earthquakes has been documented in subduction zones including Chile and Japan (Farías et al., 2011; Kato et al., 2013; Okada et al., 2015). A notable example is the Pichilemu seismic sequence following the  $M_{\rm w}$  8.8 Maule, Chile earthquake, where the largest aftershocks ( $M_{\rm w}$  6.9 and  $M_{\rm w}$  7.0) were triggered in the upper plate, accompanied by an earthquake swarm (Farías et al., 2011). In the weeks following the March 2011  $M_{\rm w}$  9.0 Tohoku-Oki Japan megathrust earthquake, swarms of crustal earthquakes were triggered in regions outside the rupture area in both the forearc and the volcanic chain (Kato et al., 2013; Okada et al., 2015). One set

<sup>\*</sup> Corresponding author.

E-mail addresses: mac716@lehigh.edu, mariahchoskins@gmail.com
(M.C. Hoskins).

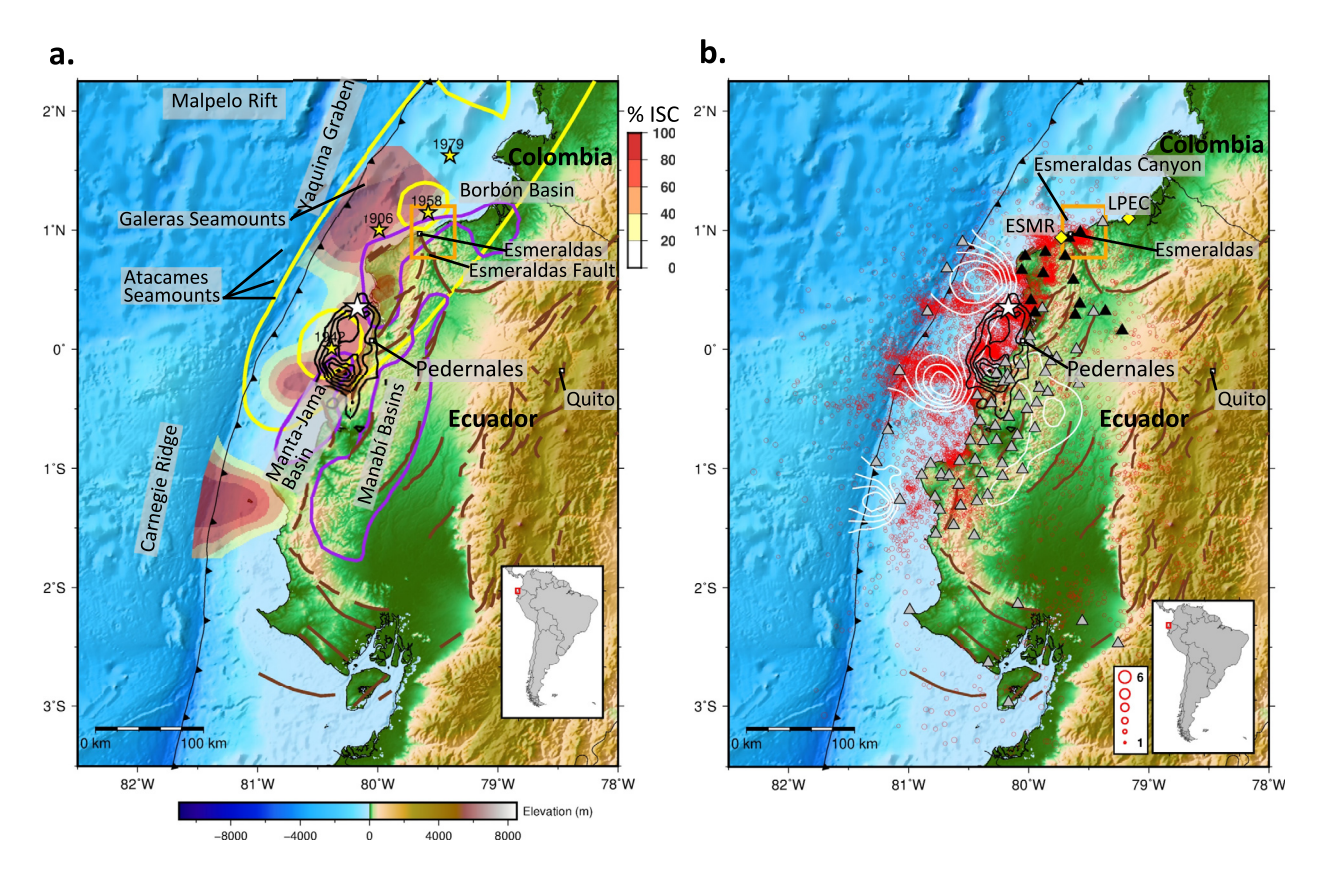


**Fig. 1.** Seismotectonic setting of Ecuador. Study area around Esmeraldas shown by orange square. Black contours are 1 m contours of coseismic slip associated with the 2016 Pedernales earthquake, with white star marking the epicenter (Nocquet et al., 2017). **a.**) Yellow ellipses show areas of maximum moment release of the 1942, 1958, and 1979 megathrust events (Swenson and Beck, 1996) and the rupture area of the 1906 megathrust event (Kelleher, 1972) (largest ellipse), with yellow stars marking the epicenters. The Carnegie Ridge, Galeras and Atacames Seamounts, Yaquina Graben, and an inactive spreading ridge are labeled. Quaternary faults are drawn in brown (Egüez et al., 2003), and major sedimentary basins are outlined in purple (Reyes, 2013). Interseismic coupling from Nocquet et al. (2014) and Collot et al. (2017) according to color scale at top right of Figure. **b.**) Map of the 2016 Pedernales rupture, aseismic slip, and aftershocks (red circles) from 17 April 2016 to 4 July 2017. Note the strong spatial clustering of aftershocks. The cluster of seismicity around Esmeraldas (orange box) is the focus of this study. Aseismic afterslip updip and downdip of the rupture and a triggered slow slip event in the south shown as white contours with a 10 cm contour interval (from Rolandone et al., 2018). Stations used for locating aftershocks are shown as gray and black triangles. Stations shown in black were used in the final 3D relocations of the events around Esmeraldas. GPS stations used in this study are shown as yellow diamonds. (For interpretation of the colors in the figure(s), the reader is referred to the web version of this article.)

of swarms culminated in the M7.0 Iwaki earthquake (Kato et al., 2013). Many of the swarms of crustal earthquakes were the result of fluid flow being triggered by changes in the stress field induced by the Tohoku-Oki megathrust earthquake (Kato et al., 2013; Okada et al., 2015).

Seismic swarms frequently occur in subduction zones (Holtkamp and Brudzinski, 2011). Seismic swarms have been linked to slow slip events (Vallée et al., 2013; Hamling and Wallace, 2015; Fasola et al., 2019) or fluid flow or high pore fluid pressure (Kato et al., 2013; Okada et al., 2015; Poli et al., 2017). The occurrence of events with similar waveforms has also been connected to high pore fluid pressure (Poli et al., 2017) or slow slip processes in subduction zone settings, such as the Ecuador-Colombia subduction zone (Vallée et al., 2013; Vaca et al., 2018).

The northern Ecuador subduction zone is characterized by heterogeneous plate coupling (Chlieh et al., 2014), caused mainly by subducting seafloor topography (Collot et al., 2017). Subducting features include the Carnegie Ridge (the track of the Galapagos Hotspot), the Atacames and Galeras seamount chains, and the Malpelo Rift, which is an inactive spreading center (Fig. 1a.) (Gutscher et al., 1999; Chlieh et al., 2014; Migeon et al., 2017). Heterogeneity in plate coupling and subducting seafloor topography are factors controlling the locations of megathrust activity and the clustering of seismicity along the north Ecuador margin (Collot et al., 2004; Font et al., 2013; Chlieh et al., 2014; Agurto-Detzel et al., 2019; Meltzer et al., 2019; Soto-Cordero et al., 2020). Variations in plate coupling are also important in slow and aseismic slip

occurring in the north Ecuador margin (Mothes et al., 2013; Vallée et al., 2013; Rolandone et al., 2018; Vaca et al., 2018).

The north Ecuador-Colombia subduction zone has hosted megathrust events both within the past century and prehistorically. Migeon et al. (2017) identified turbidite deposits from ten large earthquakes (M > 7) within the last 800 yr. In 1906, an approximately 500 km-long rupture produced a  $M_{\rm W}$  8.8 event (Kanamori and McNally, 1982; Collot et al., 2005). Subsequently, portions of that region have re-ruptured in megathrust events from south to north in 1942 ( $M_{\rm W}$  7.8), 1958 ( $M_{\rm W}$  7.7), 1979 ( $M_{\rm W}$  8.2), and 2016 ( $M_{\rm W}$  7.8) (Fig. 1a.) (Kanamori and McNally, 1982; Mendoza and Dewey, 1984; Swenson and Beck, 1996; Nocquet et al., 2017).

On 16 April 2016, the  $M_{\rm w}$  7.8 Pedernales megathrust event ruptured approximately the same area as the 1942 earthquake (Fig. 1a.) (Ye et al., 2016; Nocquet et al., 2017). Significant aseismic afterslip was identified in regions updip and downdip of the rupture of the Pedernales earthquake (Rolandone et al., 2018). Aftershocks of the Pedernales event, recorded by a combination of permanent and temporary stations, show distinct spatial clustering both south and north of the rupture and between two patches of greater slip within the rupture area (Fig. 1b.) (Rolandone et al., 2018; Agurto-Detzel et al., 2019; León-Ríos et al., 2019; Meltzer et al., 2019; Soto-Cordero et al., 2020).

Along the Ecuador subduction margin a transition occurs north of the intersection of the Carnegie Ridge with the trench. The orientation of the trench, crustal faults, and volcanic arc change from primarily north-south to northeast-southwest (Hall and Wood,

1985; Manchuel et al., 2011). The northern-most cluster of seismicity following the Pedernales earthquake is within this area, focused around the city of Esmeraldas. The Esmeraldas Fault, a major upper plate fault visible offshore as a submarine canyon, is mapped onshore along the Esmeraldas River (Hall and Wood, 1985; Egüez et al., 2003). In 1942, the segment of the subduction zone near Pedernales ruptured and was followed in 1958 with a rupture of the Esmeraldas segment (Kanamori and McNally, 1982; Mendoza and Dewey, 1984; Swenson and Beck, 1996). During the 1958 Mw 7.7 megathrust event, the Esmeraldas Fault and tectonic transition likely contributed to the southwest limit of the rupture, marking a segmentation boundary within the subduction zone (Hall and Wood, 1985; Collot et al., 2004; Manchuel et al., 2011). The seismicity clustered in the Esmeraldas area following the 2016 Pedernales earthquake is isolated to the east of the Esmeraldas Fault (Fig. 1b.).

Significant upper plate structure, including faults and accreted terranes, exist in the Ecuadorian forearc. Subduction during the Cretaceous resulted in oceanic terranes being accreted (Kerr et al., 2002). The Piñón Formation within the forearc and in the Esmeraldas area (Kerr et al., 2002; Reyes, 2013) consists of accreted oceanic crust, basalts, pillow basalts, dolerites, and gabbroic intrusions (Jaillard et al., 2009). Crustal faults trending roughly east/west cut through the Piñón Formation in the Esmeraldas area (Fig. 2) (Reyes, 2013). Additionally, the Borbón Basin, a major sedimentary basin, runs along the coastal part of the region (Fig. 1a.).

The sequence of seismicity in the Esmeraldas area following the Pedernales event is distinct both spatially and temporally from the rest of the aftershock sequence (Agurto-Detzel et al., 2019; Meltzer et al., 2019; Soto-Cordero et al., 2020). No activity was recorded in the Esmeraldas area until 2 months after the mainshock. Previously reported locations using a 1D velocity model showed that the seismicity was in the upper plate (Agurto-Detzel et al., 2019; Meltzer et al., 2019; Soto-Cordero et al., 2020). Events cluster to the northeast of the Esmeraldas Fault and reach a maximum magnitude of  $M_L$  4.9. The seismicity has clear characteristics associated with earthquake swarms, with most of the activity occurring during a twenty-five-day swarm in July 2016 (Agurto-Detzel et al., 2019; Meltzer et al., 2019; Soto-Cordero et al., 2020). The intense, shallow seismic activity caused additional damage to buildings already weakened or damaged during the Pedernales mainshock.

In this study, we relocate the events of the Esmeraldas sequence in a 3D velocity model and characterize the seismic sequence. We put the sequence in context of the tectonic and geologic setting of the region. Evidence suggests that the Esmeraldas swarm is associated with fluid flow and slow slip in the Esmeraldas area as part of the postseismic sequence of the Pedernales megathrust rupture.

#### 2. Data and methods

The seismic data used in this study is a subset from a combination of the permanent Ecuador national network (RENSIG) (Alvarado et al., 2018) and an international temporary deployment of seismic stations in response to the Pedernales event (Meltzer et al., 2019) (Fig. 1b., Sup. Fig. 1). A total of 318 events were recorded in the Esmeraldas area from the onset of seismicity on 4 June 2016 through 3 May 2017 (Sup. Fig. 2). Initial locations came from the catalog of Soto-Cordero et al. (2020), which consisted of automatic detections and earthquake location in the 1D global IASP91 (Kennett, 1991) velocity model. We then selected the 190 events of M<sub>L</sub> 2.5 or greater and manually reviewed and adjusted the existing P and S picks as necessary and made additional picks where possible (mostly S picks). We initially relocated the events using the IASP91 velocity model (Kennett, 1991) using BRTT Antelope Environmental Monitory Software<sup>®</sup>. Only events with a minimum of eight phases were included in the relocation process. We then did

a final relocation of all the events with a minimum of eight phases (including those below M<sub>L</sub> 2.5) using the maximum intersection method (MAXI) (Theunissen et al., 2012; Font et al., 2013) and the a-priori three dimensional P-wave velocity model for the Ecuador area developed by Font et al. (2013). We remeshed the velocity model to achieve a finer grid spacing of 0.5 km between nodes. Through a trial-and-error process, the 3D velocity model of Font et al. (2013) was modified (increased or decreased) beneath each station to produce station corrections. The velocity modifications were approximated assuming vertical ray paths beneath each station. (See Sup. Fig. 3 for profiles through the velocity model.) In the relocation process, we used only P-wave arrivals from 14 stations (listed in Sup. Fig. 1) within 80 km of the events, as the 3D velocity model is a P-wave-only model. To solve for a location, P arrival times at station pairs are used to build equal differential time (EDT) volumes. An EDT hyperbolic volume encompasses all nodes in a three-dimensional grid that satisfy the arrival time difference at a station pair and includes the origin location. In theory, all EDT volumes intersect at the hypocenter position. The region with the maximum intersections of EDT volumes for a given event is assessed iteratively, narrowing the volume in which the earthquake origin may be located, until finally the barycenter of the volume is chosen as the hypocenter solution. The robustness of the solution is assessed using various confidence factors, primarily Q<sub>EDT</sub>, which is a ratio of the theoretical maximum EDT volume intersections and the actual number of intersections (Font et al., 2004). High-quality locations were defined as those having a minimum number of five phases and Q<sub>FDT</sub> of at least 0.8. The average number of phases for the high-quality locations is eight, and the average Q<sub>EDT</sub> is 0.98. A total of 216 events met the criteria for high quality locations (Sup. Fig. 2). On average, horizontal and vertical errors are 0.43 and 3 km, respectively. Details on the errors are given in the Esmeraldas earthquake catalog in the Supplementary Material.

We identified episodes of swarm activity within the sequence using the full catalog of 318 events. Swarms were identified based on the criteria used by Holtkamp and Brudzinski (2011), which are 1) a period of activity visually identified as being above the background level without a mainshock triggering event, 2) the magnitudes of events vary throughout the period of heightened activity, with multiple events with less than 1 degree magnitude difference from the highest magnitude event, and 3) having a clear beginning and end to the sequence (e.g. a clear return to background levels). The rate of seismicity in the Esmeraldas area from 2011 to the time of the Pedernales earthquake recorded by the permanent national network (Alvarado et al., 2018) (Sup. Fig. 4) shows that the background levels of seismicity in the area is 0-1 event (M 1.8 to 4.4) in a day.

We calculated moment tensor solutions for eleven of the largest events M<sub>L</sub> 4.0-4.97, inverting waveforms in the 10-25 s period using the ISOLA software (Sokos and Zahradnik, 2013). In this method, we kept the epicenter fixed, while the centroid depth and origin time are solved for by grid search (Sokos and Zahradnik, 2013). The epicentral locations as determined by the refined relocations in the 1D velocity model were used for the inversion. Solutions were evaluated as high (A) and moderate (B) quality based on the values of variance reduction (A: >50; B: >40), condition number (A and B: <10), focal-mechanism variability index (A: <35; B: all values), space-time variability index (A: <0.30; B: all values), and correlation (A: >0.70; B: >0.60) (Supplementary Table 1). These thresholds are based on those suggested for evaluating solution quality in Sokos and Zahradnik (2013). Azimuthal coverage for all the events is limited, due to the stations mainly being on land and ocean-bottom seismometers (OBSs) being only west/southwest of the events (Fig. 1b.). To explore reproducibility, solutions were also calculated using the MECAVEL method (Supplementary Tables

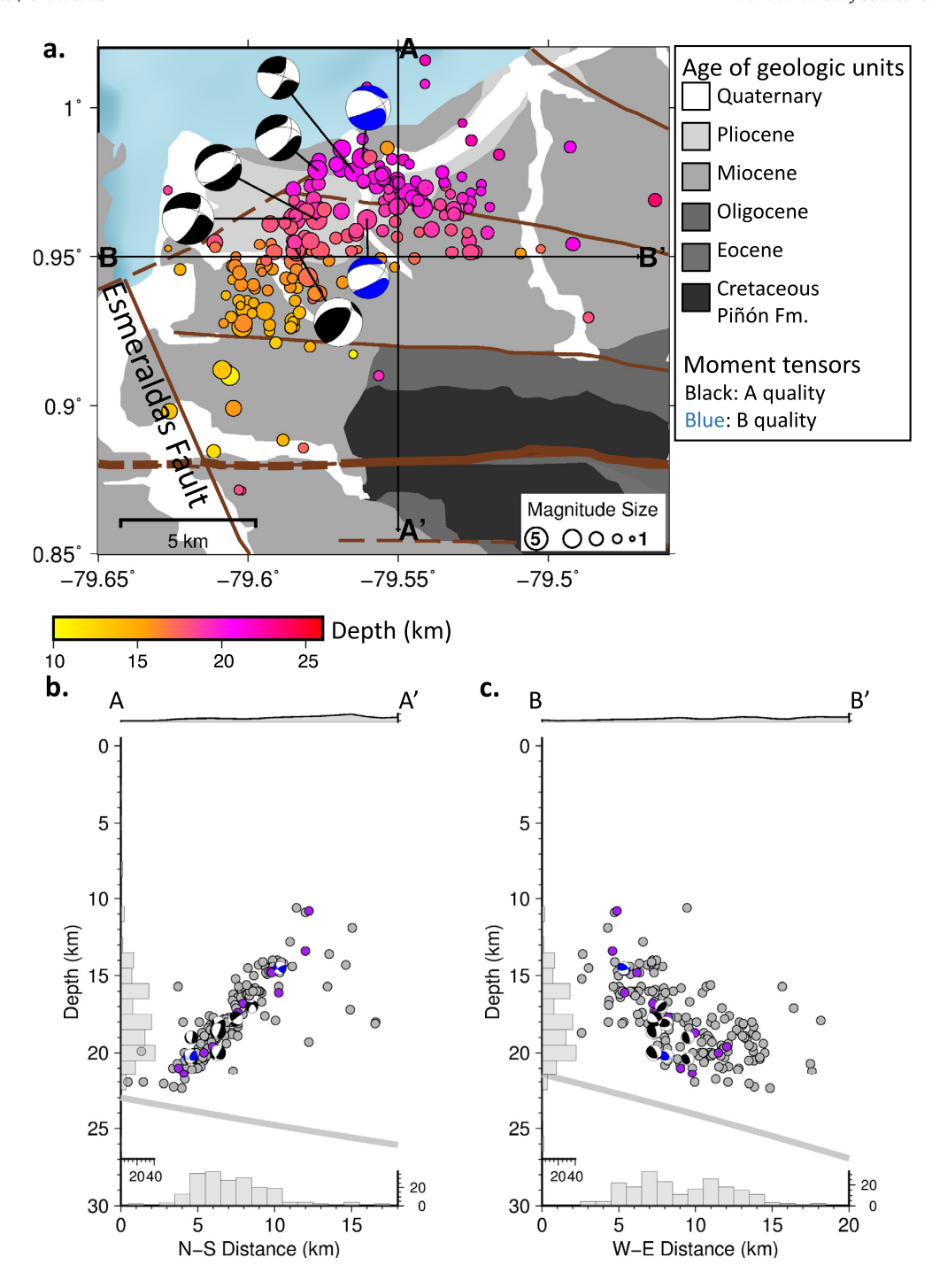


**Fig. 2.** Map of events in Esmeraldas (a) (colored by depth) and dip (b) and strike (c) cross sections. Event locations shown are the 216 high quality locations from the 3D relocation process. Compressional quadrants of focal mechanisms from moment tensor inversions are colored based on quality of the solution (black = quality A, blue = quality B). Geologic ages of the units and faults (brown) after Reyes (2013) and Egüez et al. (2003). Faults dashed were inferred. Cross sections are A-A' (dip) and B-B' (strike) based on the best-fit plane calculated through the hypocenter locations (Sup. Fig. 15). Widths of projection are 10 km on either side for line A and 8 km on either side for line B. The slab interface as modeled by Font et al. (2013) is shown as a gray line on the cross sections. Events of M<sub>L</sub> 4-4.9 (shown in purple for those events for which there is not a moment tensor solution) occur at the full depth range that smaller magnitude events do. The fault mapped at the surface which best aligns with the hypocenter locations (shown with thicker line) is in the Cretaceous Piñón Formation—an accreted oceanic terrane.

2 and 3) (Grandin et al., 2017). A GCMT solution (www.globalcmt.org) was available for one event, and was compared to the other solutions for it. The seven moment tensors that were similar between the ISOLA and MECAVEL solutions were selected as reliable, and the corresponding ISOLA solutions are presented in this study (Fig. 2 and Supplementary Table 1). For the ISOLA solutions, we tested results using two different local 1D velocity models for calculating Green's functions and found consistent results in the

moment tensor solutions (Supplementary Table 4). A 1D local velocity model (León-Ríos et al., 2019) was used for all the events. A 1D velocity model based on the one extracted from the closest node of the 3D velocity model by Font et al. (2013) was tested on three events. Additionally, we tested the effect of the epicentral location on the moment tensors by using the epicenter from the relocations in the 3D velocity model for three of the solutions. All the tests resulted in similar solutions, suggesting that minor differ-

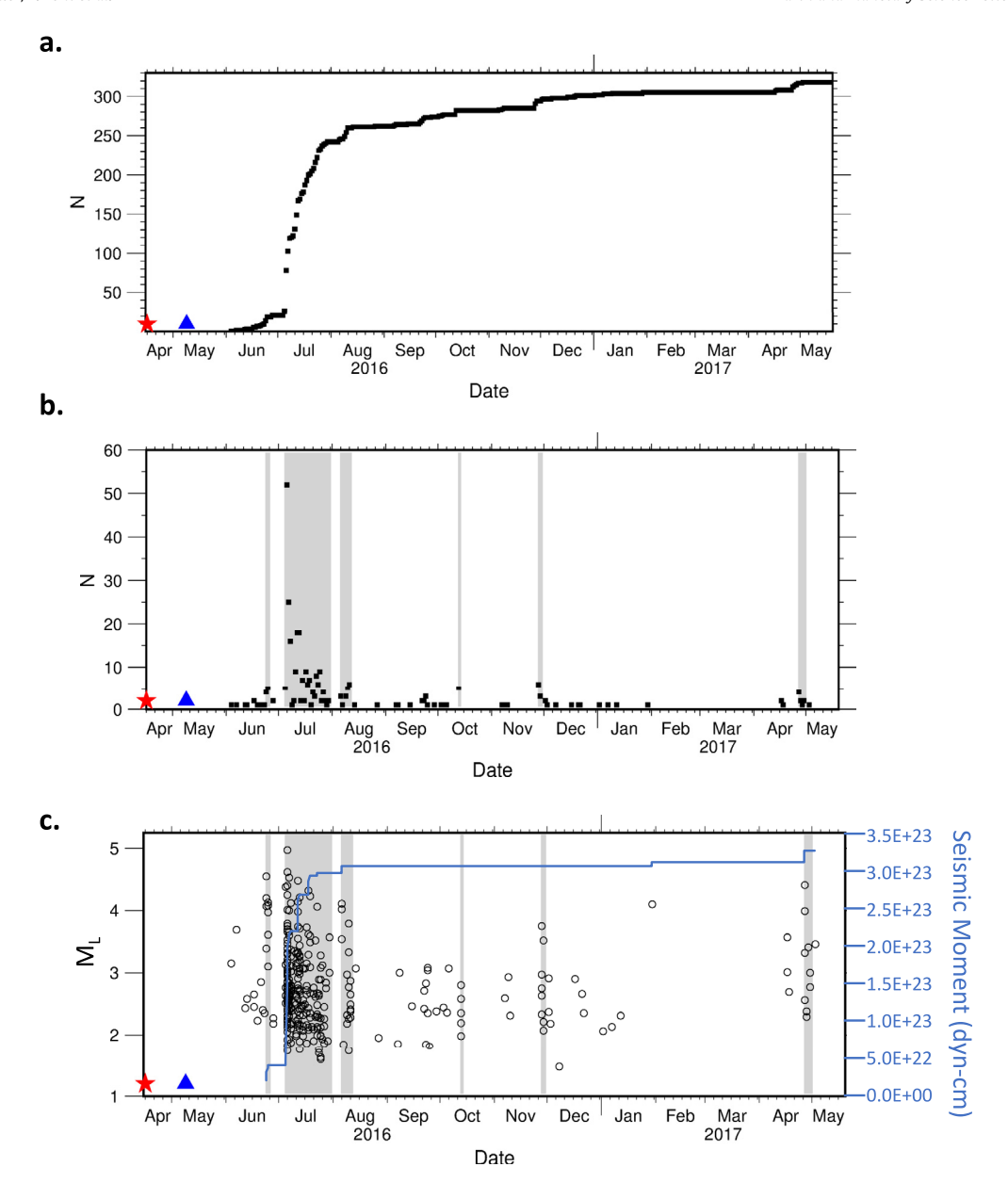


Fig. 3. Characteristics of seismicity in the Esmeraldas area over the 13 months of this study. Note the temporal variability in seismicity. Pedernales mainshock marked by red star. Blue triangle marks the start of the temporary deployment. 4a.) Cumulative number of events 4b.) Number of events per day 4c.) Magnitude (black circles) and cumulative seismic moment (blue line) vs. time. Gray shaded regions in b. and c. show timing of individual swarms within the sequence. See Fig. 4 for details of each earthquake swarm. See Sup. Fig. 4 for number of events per day in the Esmeraldas area from 2011 till the Pedernales mainshock.

ences in the epicenter location and velocity model did not affect the solutions (Supplementary Table 2). Figures showing the constraint on the solution for the seven solutions considered reliable are shown in Sup. Figs. 5-13.

To compute cumulative moment release over time, we use a linear regression to relate  $M_L$  to  $M_W$ , using the seven good-quality moment tensor solutions. We used this relation to calculate  $M_W$  for all other events down to  $M_L$  4.0 (Sup. Fig. 14). From the  $M_W$ , we calculate seismic moment using the equation of Hanks and Kanamori (1979)  $1.5M_W = \log(M_0) - 16.1$ . We use the computed seismic moment of each earthquake of  $M_L$  4.0 or greater to calculate the cumulative seismic moment shown in Fig. 3c.

We used waveform cross-correlation analysis to identify events with similar waveforms using the GISMO toolbox for MatLab (Buurman and West, 2010). Vertical component waveforms recorded by station ECO2, located immediately above the earthquake swarm (Sup. Fig. 2), were used for the cross-correlation analysis. The

waveforms were windowed from 5 seconds before to 10 seconds after each recorded P arrival. A taper was applied, and the waveforms were bandpass filtered from 0.5 to 10 Hz. After the taper and filter were applied, a further selection of the waveforms was made, from 0.2 seconds before the P arrival time to 5 seconds after. This window was selected as it encompassed the P and S waves from each event without incorporating much noise or extraneous signal. Windowing the data first with a larger and then a smaller window removes potential edge effects of the taper and filter from the cross-correlation analysis. The tapered, filtered, windowed waveforms from each event were then compared to each other. In each comparison, the waveforms were time shifted to find the maximum correlation coefficient between each pair of event waveforms. A cross-correlation coefficient of at least 0.8 was used to define similar waveforms. The cross-correlation coefficient of 0.8 was chosen based on the methods of previous studies analyzing earthquake swarms in the Ecuador margin near La Plata

Island (Vallée et al., 2013) and Mompiche (Vaca et al., 2018). This coefficient is high enough to ensure that events within a family come from a similar tectonic source and location. We additionally analyzed families of events based on a threshold cross-correlation coefficient of 0.9.

Data from two continuous GPS stations near Esmeraldas (ESMR and LPEC) (Fig. 1b.) were used in this study. One close station (RVRD) had annual transients that could not be removed, so the station is not used in this study. All other stations were too far away to record a signal from the Esmeraldas area. A test performed on the next two closest stations using synthetic computations for a fault centered on the seismic swarm and a slip with equivalent magnitude of 6.0 showed that the expected motion at those sites would be far below the resolution of the time series. GPS time series from the stations used were processed using the GAMIT/GLOBK v10.70 software after methods described in Nocquet et al. (2014). The postseismic time-series until the end of 2016 are detrended from their pre-earthquake velocity as in Rolandone et al. (2018). Additionally, a common-mode correction estimated using sites located away from the Pedernales rupture was applied, and the offset of the two 11 July 2016 (Mw 5.9 and 6.3) events which occurred about 50 km away from Esmeraldas was corrected.

To extract a local signal from the GPS time series at the ESMR and LPEC stations, we model the effect of afterslip due to the Pedernales mainshock and subtract that from the timeseries. Post-seismic time series for the Pedernales earthquake show greater dynamics than the usually observed log or exponential smooth decay, and a simple log or exponential function provides a rather poor fit. We therefore use an alternative strategy and extended the daily inversion of slip presented in Rolandone et al. (2018) to 200 days following the Pedernales earthquake, and excluded GPS sites within 50 km of the Esmeraldas seismic swarm. Such a model therefore provides a prediction of the overall contribution of afterslip to the time series at the ESMR and LPEC sites, preserving potential signals from local sources at those sites.

We used the EDCMP software (Wang et al., 2003) to calculate the Coulomb stress changes induced by (1) the coseismic slip of the 16 April 2016 mainshock using the model from Nocquet et al. (2017) (2) 30 days of afterslip as modeled by Rolandone et al. (2018), and (3) the two large aftershocks (Mw 6.7-6.9) that occurred north of the rupture on 18 May 2016. For the latter, we used a simple rectangle dislocation with the top left corner at longitude 80.06°W, latitude 0.27°N, depth 20 km, strike 24°, dip 25°, rake 117°, length and width of 50 km, and a slip of 0.5 m. Source parameters are taken from the focal mechanisms from the SCARDEC Source Time Functions Database (scardec.projects.sismo.ipgp.fr). The size of the fault and slip amount are taken from classical scaling laws for earthquakes (Wells and Coppersmith, 1994) and reflect an equivalent magnitude of 7.07, corresponding to the summed moment of both aftershocks. In the Esmeraldas area, we used receiver faults with strike 267°N and dip 43°, estimated from the best plane fitting the swarm seismicity distribution (see details about geometry of seismicity distribution in Results). Because the focal mechanisms obtained for the largest events of the seismic swarm show some dispersion, we tested rake values of  $-47^{\circ}$ , corresponding to normal-oblique focal mechanisms, and pure normal mechanisms (rake  $-90^{\circ}$ ), corresponding to the dominant mechanism during the swarm. All calculations used a standard frictional coefficient of 0.6.

#### 3. Results

Seismic activity in the Esmeraldas area started 49 days after the mainshock, and after an intense initial earthquake swarm, was sporadic throughout the year following the Pedernales event; the level of seismicity, both rate and magnitude varied (Fig. 3).

The magnitude of events recorded varies between  $M_L$  1.13-4.97 (Figs. 3c and 4). Most of the activity (221 events) is concentrated during a 26-day swarm in July 2016. Five additional small earth-quake swarms occurred between June 2016 and May 2017 consisting of 5 to 18 events and lasting 1 to 6 days (Fig. 4). In each swarm, either the largest event of the sequence occurs after the initiation of the sequence or the swarm begins with the largest event and other events occur within one unit of magnitude of the largest event. Throughout the sequence, the distribution of magnitudes is similar.

While a few individual events occurred in the Esmeraldas area beginning 4 June 2016, the first small swarm occurred 24-25 June 2016. This small swarm sequence started with an  $M_L$  4.55 event, followed by eight events ranging in magnitude from 3.1 to 4.2 over the next 36 hours.

The region experienced intense swarm activity beginning on 5 July 2016. The swarm activity continued through 30 July 2016, with 221 events recorded. Magnitudes of events varied from  $M_L$  1.59 to  $M_L$  4.97 (Fig. 4). The bulk of activity was concentrated across four days, from 5-8 July, in which 98 events were recorded. The largest magnitude event recorded in the area  $(M_L$  4.97) occurred the second day. After the first 4 days, the next days with the most activity were 11-13 July, in which 45 events were recorded (Fig. 4c.). On 11 July, two large events  $(M_W$  5.9 and 6.3) occurred  $\sim\!55$  km to the west of Esmeraldas.

A small swarm occurred 6-11 August 2016. This sequence began with an  $M_L$  4.11 event, followed by 17 events of  $M_L$  1.73 to  $M_L$  4.02. On 13 October 2016, a small swarm of five events occurred with the lowest magnitude event ( $M_L$  1.98) at the beginning of the sequence increasing in magnitude through the last event ( $M_L$  2.8). A small swarm containing nine events from 28-29 November 2016 contained events ranging from  $M_L$  2.07 to  $M_L$  3.75. The largest event occurred about halfway through the swarm. The final swarm was 27-30 April 2017 which began with an  $M_L$  4.41 event. This was followed by eight events of  $M_L$  2.29 to  $M_L$  3.99.

The high-quality 3D MAXI relocations provide detailed spatial information for many of the events during the June, July, August, and November 2016 swarms. Relocations were not able to be determined for the events in the October 2016 and April 2017 swarms because none of the events in these swarms met the criteria for high quality locations. The tightly clustered events in the Esmeraldas area are limited to an approximately 8 by 11 km area. A best-fit plane calculated through the tightly clustered hypocenter locations, using a least squares regression, results in an east-west striking plane dipping  $40^{\circ}$ N (Fig. 2 and 3D plots in Sup. Fig. 15). The hypocenters form a pipe-like distribution diagonally across the best-fit plane. Events of  $M_L$  4.0-4.97 are distributed in depth throughout the tightly clustered region (Fig. 2b. and c.).

Events within the tightly clustered area migrate over time (Fig. 5). The events in the 24-25 June swarm occur at the southwest end of the region. The July swarm begins with the first events on 5 July in the middle of the region, closer to the northeastern part of it. The event hypocenters spread out during the next 23 days, as shown in Fig. 6, with some occurring near the first event hypocenter, but with an overall increasing distance from the first event. Linear regressions through the data of distance from first hypocenter versus time from days 0-5 shows a rate of expansion of hypocenter distribution of nearly 500 m/day ( $R^2 = 0.11$ ). The linear regression through the remaining 18 days of the July swarm (beginning at the time of an event located near the first event) shows a rate of expansion of about 200 m/day ( $R^2 = 0.21$ ). A single regression through all the events in July results in an expansion rate of 176 m/day ( $R^2 = 0.27$ ). Events in the 6-11 August swarm are more scattered, locating in the outskirts of the clustered region. The events occurring in the 28-29 November swarm are isolated to the northeastern part of the region.

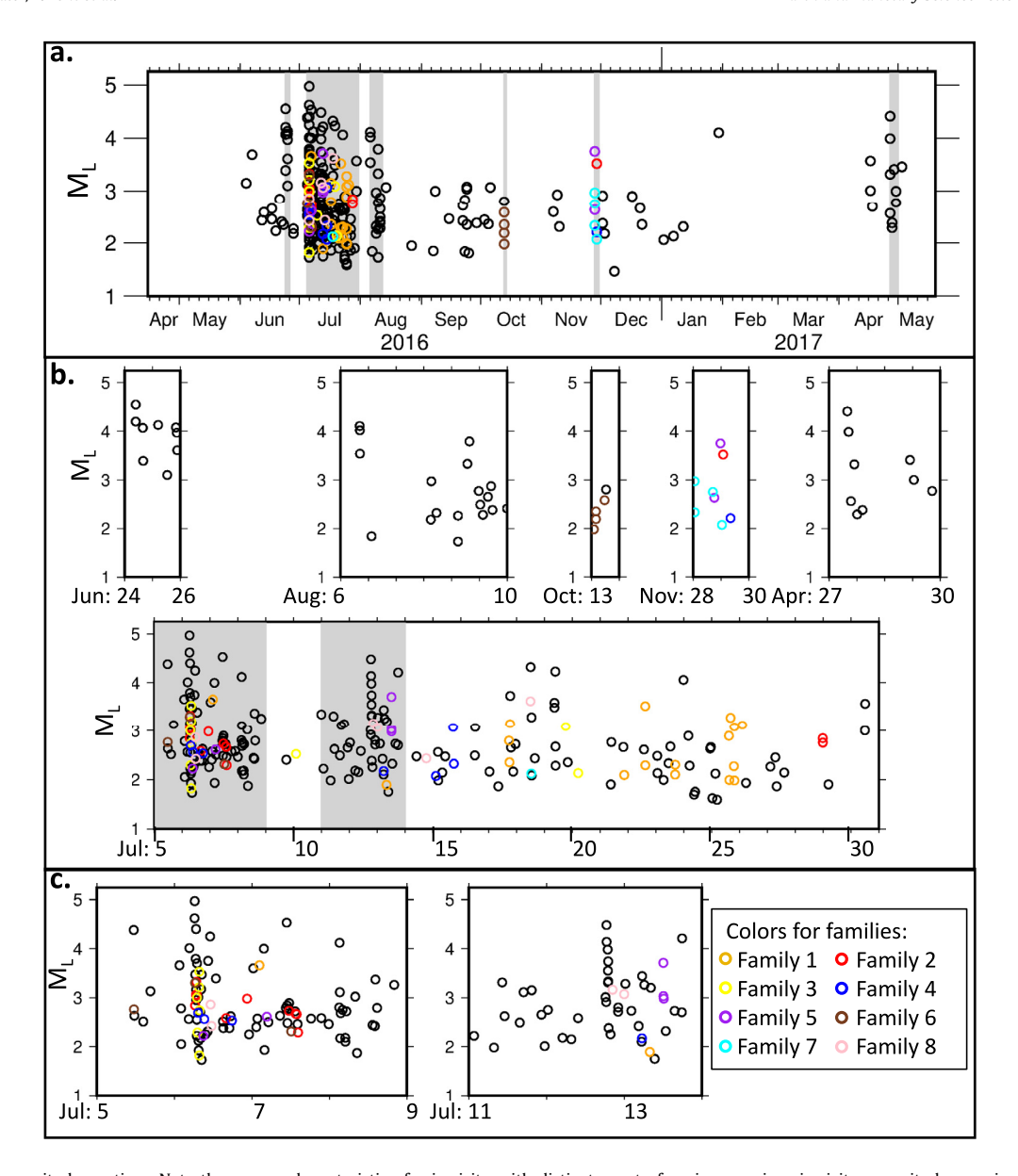
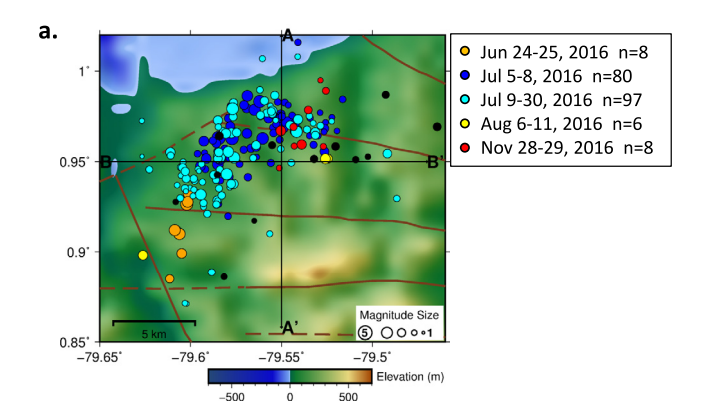


**Fig. 4.** Earthquake magnitude vs. time. Note the swarm characteristic of seismicity with distinct onset of an increase in seismicity, magnitudes varying within an order of magnitude throughout each swarm, and the largest magnitude event occurring within the sequence. Events occurring in families of related events color-coded according to legend. All other events shown in black. The events with similar waveforms are mostly limited to the July 2016 swarm. The entire 13 months period discussed in the text are shown in **a.**, with gray boxes highlighting the swarms. Earthquake swarms in **5a.** (gray boxes) expanded in **5b.** Swarm activity in **5b.** (gray boxes: July 5-9 and 11-13) expanded in **5c.** 

Moment tensor inversions resulted in reliable solutions for seven events within the July 2016 swarm with M<sub>w</sub> 3.8-4.6 (Fig. 2). The moment tensors show a variety of geometries in the nodal planes: five events indicate normal or oblique normal faulting, one shows a strike-slip motion, and one shows reverse motion. The double-couple component for the solutions ranges from 51% to 96%. The four solutions with the lowest double couple had 72%, 62%, 52%, and 51% double couple. In order to respect the pointsource assumption, the two stations closest to the events (EC01 and EC02, <10 km epicentral distance) were not considered for the inversion. We present details on the waveform fit and constraint of the moment tensor solutions in Sup. Figs. 5-13. Although the double-couple component is not completely reliable on its own, we present these results and interpret them together with the more well-constrained focal mechanisms calculated for the moment tensors.

Eight families comprised of at least six related events were identified by waveform correlation, using a cross-correlation coeffi-

cient of at least 0.8 to define a family. The temporal distribution of the events in families is shown in Fig. 4, while the spatial distribution is shown in Fig. 7. Waveform plots of related events are shown in Sup. Figs. 16 and 17). All the families were initiated during the July 2016 swarm; all but one of the families (family 7) were initiated during the first four days of the swarm (5-8 July). Most of the well-correlated events are confined to the July swarm. Four families also contain events occurring after 30 July 2016 (Fig. 4). Four families contain well-correlated events during the October and November swarms. Some events locate within 0.1 km of another event in the same family. Most events within each family locate within 2 km epicentral distance of each other, with the farthest spread in the high-quality locations being 5 km (in families 1 and 5) (Fig. 7). Families of events identified using a threshold cross-correlation coefficient of 0.9 (Sup. Figs. 18-20) show some events within families with 0.1-0.2 km of each other. Most are within 1 km of other events in the family, and some are up to 2.8 km apart.



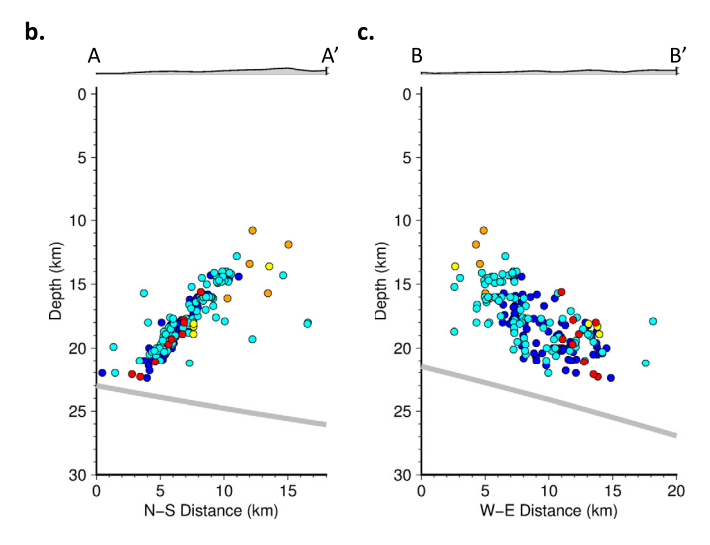


**Fig. 5.** Events in Esmeraldas area (216 high quality locations), color-coded by the swarm in which they occur. Note the spatial clustering of most of the events within each swarm. Cross sections and faults are the same as in Fig. 2. Fewer events are shown for each time period than are reported in the description of the swarms because only the high-quality locations are being shown in this Figure.

The time-series of two close GPS stations (ESMR and LPEC) predominantly show an exponential decay related to the postseismic deformation after the Pedernales earthquake. Superimposed on this signal, an anomalous signal is seen in the east component of the GPS time-series beginning synchronously with the onset of seismicity on 4 June 2016 (Fig. 9). The anomalous signal shows first a deceleration of the westward motion. It is then followed by a transient acceleration during the July 2016 swarm, progressively vanishing in August. The transient observed may be related to a slow slip event on the plate interface or to a slow slip event on the crustal fault imaged by the earthquake hypocenters.

To investigate the source of the slip causing the transient, we removed the signal of the afterslip from the Pedernales event (as described in the Methods section). The residual time series (Observed-Modeled) (Fig. 8) shows an eastward transient. The magnitude of the signal is small at  $\sim\!\!4$  mm in the east component of ESMR. Modeling of slip on a crustal normal fault with strike 267°N, dip 43°, and rake  $-90^\circ$  (the geometry of the best-fit plane calculated through the hypocenters) shows that the expected signal is consistent with the observed transient. Modeling of slip on crustal fault with the given geometry and assuming a fault plane length of 11 km and width of 15 km and slip of 200 mm (details in Sup. Fig. 21), results in a predicted GPS transient corresponding to an equivalent magnitude of about six, which is compatible with the transient observed.

Coulomb stress modeling, using receiver faults with the geometry indicated by the swarm event hypocenter distribution show

Coulomb stress changes were positive for the Pedernales coseismic slip and for the two 18 May 2016 ( $M_{\rm W}$  6.7-6.9) aftershocks (Fig. 9). Coulomb stress was close to zero for the afterslip in the first 30 days following the mainshock. The tests using a rake value of  $-47^{\circ}$  and  $-90^{\circ}$  (normal fault) both resulted in positive Coulomb stress changes of  $\sim\!0.3$  Bar. The Coulomb stress changes after the Pedernales earthquake and large aftershocks favored the normal and normal-oblique slip indicated by the focal mechanisms along the identified fault.

#### 4. Discussion

Event hypocenters from the Esmeraldas sequence locate above the plate interface as modeled by either Slab 2 (Hayes, 2018) or Font et al. (2013). The slab model of Font et al. (2013) aligns with the base of seismicity (Fig. 2), while the Slab 2 model is  $\sim\!13$  km deeper. The Font et al. (2013) model is therefore the preferred slab model in this region. Events, including those of  $M_L$  4.0-4.97, occur from just above the plate interface at 22 km depth to as shallow as 10 km depth (Fig. 2). Events with lower quality relocations occur as shallow as 3 km.

The Esmeraldas sequence is characterized by earthquake swarms, particularly the 26-day swarm in July 2016 (Fig. 3). In other areas in Ecuador, earthquake swarms are frequently observed in association with slow slip events and have been used as proxies for identifying past slow slip events (Vallée et al., 2013; Rolandone et al., 2018). In the New Zealand subduction zone, an earthquake swarm triggered in the upper plate by a slow slip event at the interface was documented by Hamling and Wallace (2015). In Mexico, along strike motion of slow slip events has been documented in crustal earthquake swarms occurring during slow slip events (Fasola et al., 2019). In Japan, swarms of earthquakes lasting several weeks occurred in the upper plate following the Tohoku-Oki megathrust earthquake (Okada et al., 2015). Events in some of these swarms exhibited an increasing trend of event hypocenter distance from the first event. Based on models of fluid diffusion, the expansion of the earthquake swarm area marks the fluid diffusion front as fluids move out from a region of high pore fluid pressure (Okada et al., 2015). In the Esmeraldas sequence, the increasing trend of event hypocenter distance from the first event (Fig. 6) is similar to what Okada et al. (2015) described in earthquake swarms in Japan that lasted several weeks. Rates of expansion of the hypocenter region in Esmeraldas, based on linear regression through the data of distance from first event versus time, give rates of about 500 m/day for the first five days and about 200 m/day after that (Fig. 6). The low  $R^2$  value of the regression and the distribution of the distance of hypocenters over time, including multiple later events locating near the initial event, suggests fluid pulses and variable migration rates. Migration rates of hypocenters in crustal earthquake swarms vary widely. Examples include rates of 105 m/day representing fluid migration rates (Nippress and Rietbrock, 2007) and 2-4.6 km/day representing a slow slip front (Fasola et al., 2019). The calculated rates for the Esmeraldas sequence fit within this range, and are closer to the rates found for a sequence in Chile that represented fluid flow (Nippress and Rietbrock, 2007), but as mentioned, the spatiotemporal distribution of the seismicity suggests multiple pulses of fluids.

The normal and strike-slip moment tensor solutions for events in the Esmeraldas sequence (Fig. 2) are consistent with high pore fluid pressure causing increased extensional stress in the crust and decreasing the frictional strength of existing faults (Kato et al., 2013). While less well-constrained than the sense of motion, the non-double-couple component found in some moment tensors is also consistent with seismicity linked to high pore fluid pressure (Julian et al., 1998; Kato et al., 2013). This is similar to what was observed in normal faulting, upper crustal earthquake swarms fol-

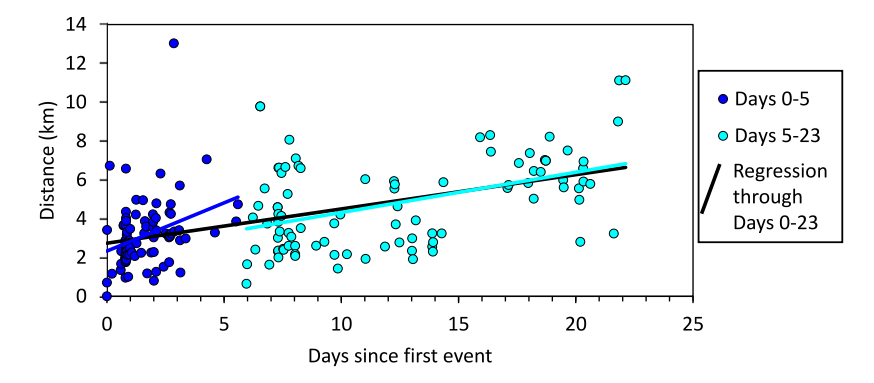


**Fig. 6.** Plot of distance from first event vs. time for events occurring in the 5-30 July 2016 swarm. Horizontal axis shows time since the first event. Events in the first five days until an event occurred close to the first event, are shown in dark blue. The events during the rest of the swarm are shown in cyan. Linear regressions through these two periods of activity and through all the events show an increasing trend in distance with time, indicating a spreading out of hypocenters over time. Linear regression through days 0-5 (blue line) shows an expansion rate of 500 m/day, regression through days 5-23 (cyan line) shows a rate of 200 m/day, and a regression through days 0-23 (black line) shows an expansion rate of 176 m/day.

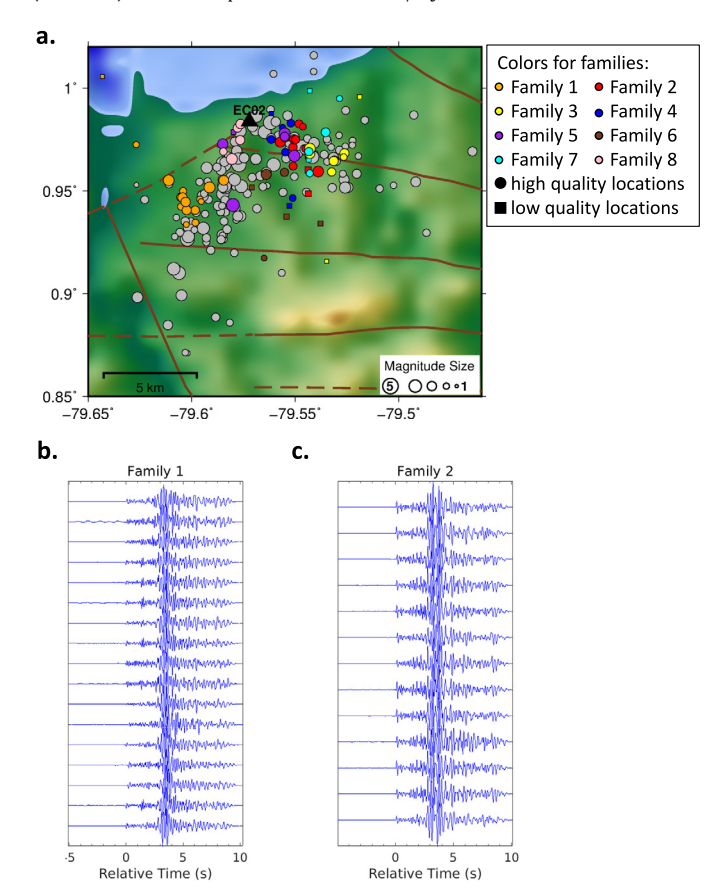


**Fig. 7.** Map of events in the Esmeraldas area colored by family of related events. Waveforms of the events within the two largest families are shown in **b.** and **c.** Waveform plots show the Z component from station ECO2. Events within the same family tend to locate near one another. Faults same as Fig. 2. Elevation colored same as Fig. 5.

lowing the Tohoku-Oki, Japan megathrust earthquake (Kato et al., 2013). The swarm behavior of seismicity in the Esmeraldas area and the moment tensors found suggests high pore fluid pressure, fluid flow and/or slow slip were the direct causes of the seismicity (Kato et al., 2013; Vallée et al., 2013; Hamling and Wallace, 2015; Okada et al., 2015; Poli et al., 2017; Rolandone et al., 2018; Vaca et al., 2018).

In the Esmeraldas sequence, the occurrence of families of events with similar waveforms (Figs. 4 and 7) is consistent with slow slip in Ecuador (Vallée et al., 2013; Rolandone et al., 2018;

Vaca et al., 2018) and in other subduction zones (Poli et al., 2017). The range of distances between events within families indicates that families potentially include repeaters and events triggered nearby, rather than necessarily being limited to true repeaters as described by Kato et al. (2013).

The observation of an anomalous signal in the two nearest GPS station time series at the initiation of seismicity and during the main swarm further suggests influence of slow slip (Fig. 8). Extraction of the afterslip of the Pedernales mainshock and modeling of motion on the imaged crustal fault show that the transient in the GPS time series is consistent with slip on the crustal fault (Sup. Fig. 21). We interpret the transient as indicating a slow slip event occurring on a crustal fault.

The same characteristics that suggest the influence of slow slip and/or fluid flow in the Esmeraldas sequence have been documented previously in the Ecuador margin. A transient signal in a GPS station near Esmeraldas in 2008 has been interpreted as indication of slow slip (Mothes et al., 2013). Earthquake swarms and repeating events have been associated with the instances of slow slip in the south around La Plata Island and offshore near Mompiche (Vallée et al., 2013; Rolandone et al., 2018; Segovia et al., 2018; Vaca et al., 2018).

The increased Coulomb stress calculated based on the location and geometry of the fault outlined by the seismicity in Esmeraldas is consistent with the seismicity being triggered by the Pedernales mainshock and the two large aftershocks on 18 May 2016 (Fig. 9). Event hypocenters outline a north-dipping, upper plate fault or shear zone (Fig. 3 and Sup. Fig. 15), indicating fluid flow and slow slip processes triggering seismicity on an upper plate fault. The increased Coulomb stress calculated based on the location and geometry of the fault outlined by the seismicity in Esmeraldas is consistent with the seismicity being triggered by the Pedernales mainshock and the two large aftershocks on 18 May 2016. The strike and location of the fault, based on hypocenter locations, aligns with faults mapped by Reyes (2013) that offsets individual blocks of the Piñón Formation (Fig. 2), which is an accreted oceanic basaltic unit (Kerr et al., 2002; Reyes, 2013). The blocks of the Piñón Formation are exposed in the Businga Dome and are unconformably overlain by sediments (Reyes, 2013). This alignment with mapped faults suggests a scenario of fluid escape along a trend following the fabric of existing structure (Fig. 10).

In central Ecuador, the alignment of seismicity with the Piñón Formation was observed in the interseismic period by Segovia et al. (2018). In other regions of the Pedernales aftershock sequence, the alignment of seismicity with faults that border the Piñón Formation is also seen (Soto-Cordero et al., 2020).

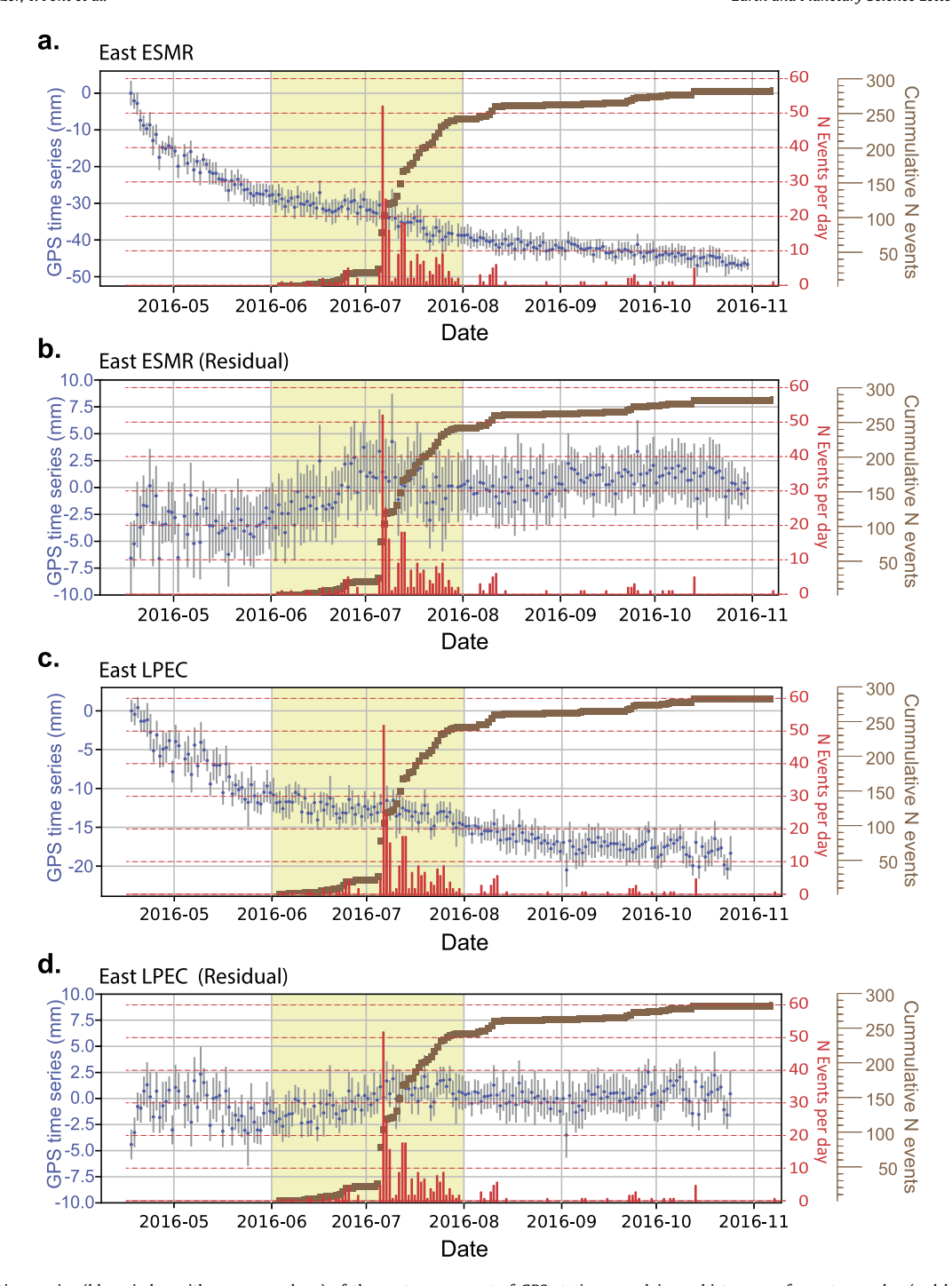
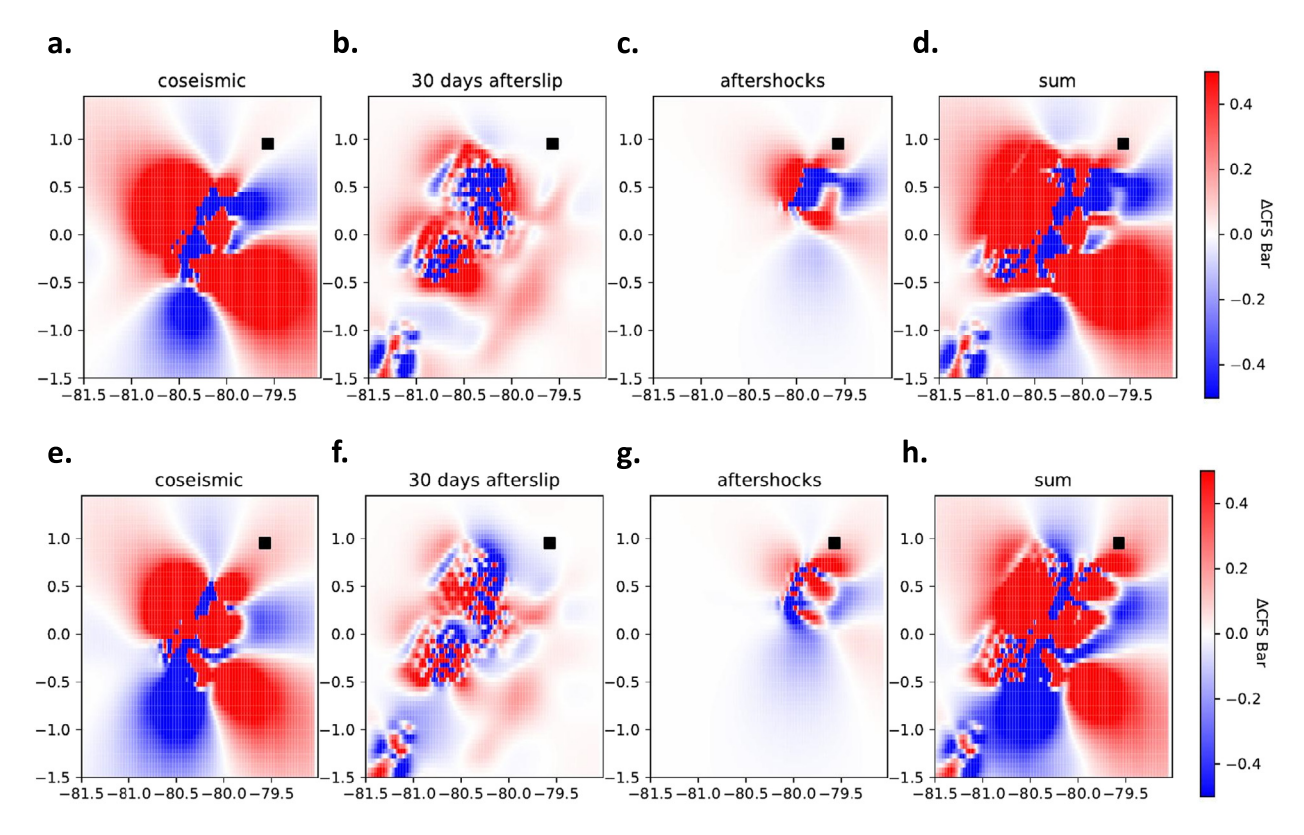


Fig. 8. Postseismic time-series (blue circles with gray error bars) of the east component of GPS stations overlain on histogram of events per day (red bars) and cumulative number of events (brown squares). East components of ESMR (a.) and LPEC (c.), starting just after the Pedernales earthquake. Common-mode correction is applied and the signal from two large 11 July 2016 aftershocks removed. The time series predominantly show an exponential decay related to the postseismic deformation of the Pedernales earthquake. The timing of the anomalous signal is shaded yellow. Residual time series (Observed-Modeled) with respect to the prediction of afterslip at the subduction interface are shown in b. and d. Locations of stations are shown in Fig. 1b.

The Esmeraldas Fault, a major upper plate fault to the southwest of the Esmeraldas clustered seismicity, is considered an important factor in the segmentation of the northern Ecuador subduction zone, separating the segment that ruptured in 1958 from the segment that ruptured in 1942 and 2016 (Fig. 1a.) (Swenson and Beck, 1996; Collot et al., 2004; Manchuel et al., 2011). Despite the separation of the subduction zone segments across the Esmeraldas Fault, the Pedernales earthquake triggered seismicity on upper plate faults in the Esmeraldas area. This demonstrates the potential of megathrust earthquakes and ensuing slow slip to

trigger fluid flow, variable slip modes, and destructive seismicity across subduction zone segment boundaries and within the shallow upper plate far from the coseismic rupture area. It is also possible that deeper events near the plate interface are the result of stress transfer from the shallower coupled (more resistant) part of the fault to a transitional weaker segment. If this is the case, it is possible there is potential for a sequence similar to the 1942 and 1958 megathrust ruptures to occur again.

The identification of active shallow upper plate faults in the Esmeraldas area by the high-quality 3D locations of the events an-



**Fig. 9.** Coulomb stress changes at a depth of 18.8 km, black square is the receiver fault. The depth of 18.8 km is where the greatest number of swarm events occur. Upper panel (**a.** through **d.**) shows stress changes for a normal oblique slip fault with strike  $267^{\circ}$ N, dip  $43^{\circ}$ , rake  $-47^{\circ}$ . Lower panel (**e.** through **h.**) shows the same calculations for pure normal slip (rake  $-90^{\circ}$ ). Coulomb stress changes induced by: the Pedernales earthquake (**a.** and **e.**), 30 days of afterslip (**b.** and **f.**), the two large May 18 aftershocks (**c.** and **g.**), and the sum of the mainshock, afterslip, and two large aftershocks (**d.** and **h.**).

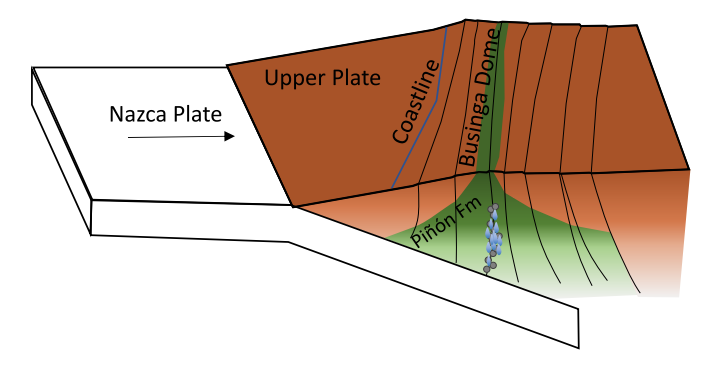


**Fig. 10.** Schematic diagram showing Esmeraldas seismicity (gray circles) relative to mapped faults (black lines) and subduction. Pore fluid in crustal fault shown as blue tear-drops. (Diagram not to scale.) Placement of faults and Piñón Formation (green) after Reyes (2013).

alyzed in this study is important in the seismic hazard assessment in the Esmeraldas area. The current model for seismic hazard in the Esmeraldas area considers only the seismic potential of the plate interface (Beauval et al., 2018). The results of this study also show the importance of understanding the seismic potential of shallow upper plate faults in subduction zones globally.

#### 5. Conclusion

The Pedernales megathrust earthquake triggered seismicity on upper plate faults or a shear zone in the Piñón Formation in the Esmeraldas area, far from the coseismic rupture area in a separate segment of the subduction zone. Positive Coulomb stress change is consistent with the earthquake swarm being triggered by the Pedernales mainshock and the two large 18 May 2016 aftershocks. Evidence for a slow slip event and for fluid flow associated with

the Esmeraldas sequence following the 2016 Pedernales megathrust earthquake are suggested by earthquake swarms. Additional evidence for fluid flow from areas of high pore pressure includes the increasing distance of event hypocenters from the first event during the main swarm and normal and strike-slip moment tensor solutions with low double-couple component. The hypocenter distribution suggests the fluid escape followed existing structural fabric. Additional evidence for a triggered crustal slow slip event in the Esmeraldas area includes the presence of events with similar waveforms and an anomalous GPS signal consistent with slip on a crustal fault. Seismic hazard assessment in regions of subduction zones should include the effects of shallow upper plate seismicity and the potential for triggering of shallow seismicity across separate segments of the subduction zone. Seismic swarms along an upper plate fault, with local magnitudes up to 4.97 caused additional damage to buildings in the Esmeraldas area following the Pedernales megathrust earthquake.

### **CRediT authorship contribution statement**

Mariah C. Hoskins: Formal analysis, Investigation, Validation, Visualization, Writing - original draft. Anne Meltzer: Conceptualization, Funding acquisition, Investigation, Project administration, Resources, Writing - review & editing. Yvonne Font: Formal analysis, Investigation, Software, Writing - review & editing. Hans Agurto-Detzel: Formal analysis, Investigation, Validation, Writing - review & editing. Sandro Vaca: Formal analysis, Investigation, Validation, Writing - review & editing. Frederique Rolandone: Formal analysis, Investigation, Writing - review & editing. Jean-Mathieu Nocquet: Formal analysis, Investigation, Writing - review & editing. Lillian Soto-Cordero: Data curation, Investigation, Writing - review & editing. Joshua C. Stachnik: Data curation, Investigation, Software. Susan Beck: Funding acquisition, Investigation, Writing

- review & editing. Colton Lynner: Investigation, Writing - review & editing. Mario Ruiz: Investigation, Supervision, Writing - review & editing. Alexandra Alvarado: Investigation, Supervision. Stephen Hernandez: Investigation, Writing - review & editing. Philippe Charvis: Investigation. Marc Regnier: Investigation. Sergio Leon-Rios: Investigation. Andreas Rietbrock: Investigation, Writing - review & editing.

#### **Declaration of competing interest**

The authors declare that they have no known competing financial interests or personal relationships that could have appeared to influence the work reported in this paper.

#### Acknowledgements

Thanks to the research and technical staff at Instituto Geofisico at the Escuela Politécnica Nacional (IG-EPN) in Quito Ecuador for excellent logistics and field support; the numerous host families in Esmeraldas and Manabí province for interest in our work and for providing station security during the deployment. Thanks to the PASSCAL facility of the Incorporated Research Institutions for Seismology (IRIS) for supporting instrumentation used in the US portion of the aftershock deployment. Additional instrumentation came from Instituto Geofísico at the Escuela Politécnica Nacional (IG-EPN) in Quito Ecuador, L'Institut de recherche pour le développement (IRD) Géoazur in Nice France, and University of Liverpool UK, with financial support from IG-EPN, IRD, CNRS, and NERC. Funding: This work was supported by The National Science Foundation NSF RAPID Program Award EAR-1642498 and NSF Geophysics Program Awards EAR-1723042 and EAR-1723065. Hans Agurto-Detzel acknowledges support from IRD/ANR project ANR-15-CE04 and UCA/JEDI project ANR-15-IDEX-01. Information about BRTT Antelope software can be found at http://www.brtt.com (last accessed October 2019). Generic Mapping Tools v5.2.1 (http:// gmt.soest.hawaii.edu/) was used for making maps and figures. We also thank the editor Jean-Philippe Avouac and reviewer J. Jara and two anonymous reviewers for insightful comments and help in improving the manuscript.

## Appendix A. Supplementary material

Supplementary material related to this article can be found online at https://doi.org/10.1016/j.epsl.2020.116620.

#### References

- Agurto-Detzel, H., Font, Y., Charvis, P., Regnier, M., Rietbrock, A., Ambrois, D., Paulatto, M., Alvarado, A., Beck, S., Courboulex, F., De Barros, L., Deschamps, A., Hernandez, M.J., Hernandez, S., Hoskins, M., Leon-Rios, S., Lynner, C., Meltzer, A., Mercerat, E.D., Michaud, F., Nocquet, J.M., Rolandone, F., Ruiz, M., Soto-Cordero, L., 2019. Ridge subduction and afterslip control aftershock distribution of the 2016 M<sub>w</sub> 7.8 Ecuador earthquake. Earth Planet. Sci. Lett. 520, 63–76. https://doi.org/10.1016/j.epsl.2019.05.029.
- Alvarado, A., Ruiz, M., Mothes, P., Yepes, H., Segovia, M., Vaca, M., Ramos, C., Enríquez, W., Ponce, G., Jarrín, P., Aguilar, J., Acero, W., Vaca, S., Singaucho, J.C., Pacheco, D., Córdova, A., 2018. Seismic, volcanic, and geodetic networks in Ecuador: building capacity for monitoring and research. Seismol. Res. Lett. 89, 432–439. https://doi.org/10.1785/0220170229.
- Beauval, C., Marinière, J., Yepes, H., Audin, L., Nocquet, J.M., Alvarado, A., Baize, S., Aguilar, J., Singaucho, J.C., Jomard, H., 2018. A new seismic hazard model for Ecuador. Bull. Seismol. Soc. Am. 108, 1443–1464. https://doi.org/10.1785/0120170259.
- Buurman, H., West, M.E., 2010. Seismic precursors to volcanic explosions during the 2006 eruption of Augustine volcano. In: Power, J.A., Coombs, M.L., Freymueller, J.T. (Eds.), 2006 Erupt. Augustine Volcano, Alaska. U.S.G.S. Prof. Pap. 1769, pp. 41–57.
- Chlieh, M., Mothes, P.A., Nocquet, J.M., Jarrin, P., Charvis, P., Cisneros, D., Font, Y., Collot, J.Y., Villegas-Lanza, J.C., Rolandone, F., Vallée, M., Regnier, M., Segovia, M.,

- Martin, X., Yepes, H., 2014. Distribution of discrete seismic asperities and aseismic slip along the Ecuadorian megathrust. Earth Planet. Sci. Lett. 400, 292–301. https://doi.org/10.1016/j.epsl.2014.05.027.
- Collot, J.Y., Marcaillou, B., Sage, F., Michaud, F., Agudelo, W., Charvis, P., Graindorge, D., Gutscher, M.A., Spence, G., 2004. Are rupture zone limits of great subduction earthquakes controlled by upper plate structures? Evidence from multichannel seismic reflection data acquired across the northern Ecuador-southwest Colombia margin. J. Geophys. Res. B, Solid Earth 109, 1–14. https://doi.org/10.1029/2004|B003060.
- Collot, J.Y., Migeon, S., Spence, G., Legonidec, Y., Marcaillou, B., Schneider, J.L., Michaud, F., Alvarado, A., Lebrun, J.F., Sosson, M., Pazmino, A., 2005. Seafloor margin map helps in understanding subduction earthquakes. Eos 86. https:// doi.org/10.1029/2005E0460003.
- Collot, J.Y., Sanclemente, E., Nocquet, J.M., Leprêtre, A., Ribodetti, A., Jarrin, P., Chlieh, M., Graindorge, D., Charvis, P., 2017. Subducted oceanic relief locks the shallow megathrust in central Ecuador. J. Geophys. Res., Solid Earth 122, 3286–3305. https://doi.org/10.1002/2016JB013849.
- Egüez, A., Alvarado, A., Yepes, H., Machette, C.C., Dart, R.L., 2003. Database and map of Quaternary faults and folds of Ecuador and its offshore regions. USGS Open-File Report 03-289.
- Farías, M., Comte, D., Roecker, S., Carrizo, D., Pardo, M., 2011. Crustal extensional faulting triggered by the 2010 Chilean earthquake: the Pichilemu seismic sequence. Tectonics 30, 1–11. https://doi.org/10.1029/2011TC002888.
- Fasola, S.L., Brudzinski, M.R., Holtkamp, S.G., Graham, S.E., Cabral-Cano, E., 2019. Earthquake swarms and slow slip on a sliver fault in the Mexican subduction zone. Proc. Natl. Acad. Sci. USA 116, 7198–7206. https://doi.org/10.1073/pnas. 1814205116.
- Font, Y., Kao, H., Lallemand, S., Liu, C.S., Chiao, L.Y., 2004. Hypocentre determination offshore of eastern Taiwan using the maximum intersection method. Geophys. J. Int. 158, 655–675. https://doi.org/10.1111/j.1365-246X.2004.02317.x.
- Font, Y., Segovia, M., Vaca, S., Theunissen, T., 2013. Seismicity patterns along the Ecuadorian subduction zone: new constraints from earthquake location in a 3-D a priori velocity model. Geophys. J. Int. 193, 263–286. https://doi.org/10.1093/gii/ggs083.
- Grandin, R., Vallée, M., Lacassin, R., 2017. Rupture process of the M<sub>w</sub> 5.8 Pawnee, Oklahoma, earthquake from sentinel-1 InSAR and seismological data. Seismol. Res. Lett. 88, 994–1004. https://doi.org/10.1785/0220160226.
- Gutscher, M.A., Malavieille, J., Lallemand, S., Collot, J.Y., 1999. Tectonic segmentation of the North Andean margin: impact of the Carnegie ridge collision. Earth Planet. Sci. Lett. 168, 255–270. https://doi.org/10.1016/S0012-821X(99)00060-6.
- Hall, M.L., Wood, C.A., 1985. Volcano-tectonic segmentation of the northern Andes. Geology 13, 203–207. https://doi.org/10.1130/0091-7613(1985)13<203:VSOTNA> 2.0.CO:2.
- Hamling, I.J., Wallace, L.M., 2015. Silent triggering: aseismic crustal faulting induced by a subduction slow slip event. Earth Planet. Sci. Lett. 421, 13–19. https://doi.org/10.1016/j.epsl.2015.03.046.
- Hanks, T.C., Kanamori, H., 1979. A moment magnitude scale. J. Geophys. Res. 84, 2348–2350. https://doi.org/10.1029/JB084iB05p02348.
- Hayes, G., 2018. Slab2 A Comprehensive Subduction Zone Geometry Model.
- Holtkamp, S.G., Brudzinski, M.R., 2011. Earthquake swarms in circum-Pacific subduction zones. Earth Planet. Sci. Lett. 305, 215–225. https://doi.org/10.1016/j.epsl.2011.03.004.
- Jaillard, E., Lapierre, H., Ordoñez, M., Álava, J.T., Amórtegui, A., Vanmelle, J., 2009. Accreted oceanic terranes in Ecuador: southern edge of the Caribbean Plate? Geol. Soc. (Lond.) Spec. Publ. 328, 469–485. https://doi.org/10.1144/sp328.19.
- Julian, B.R., Miller, A.D., Foulger, G.R., 1998. Non-double-couple earthquakes 1. Theory. Rev. Geophys. 36, 525–549.
- Kanamori, H., McNally, K.C., 1982. Variable rupture mode of the subduction zone along the Ecuador-Colombia coast. Bull. Seismol. Soc. Am. 72, 1241–1253.
- Kato, A., Igarashi, T., Obara, K., Sakai, S., Takeda, T., Saiga, A., Iidaka, T., Iwasaki, T., Hirata, N., Goto, K., Miyamachi, H., Matsushima, T., Kubo, A., Katao, H., Yamanaka, Y., Terakawa, T., Nakamichi, H., Okuda, T., Horikawa, S., Tsumura, N., Umino, N., Okada, T., Kosuga, M., Takahashi, H., Yamada, T., 2013. Imaging the source regions of normal faulting sequences induced by the 2011 M9.0 Tohoku-Oki earthquake. Geophys. Res. Lett. 40, 273–278. https://doi.org/10.1002/grl.50104.
- Kelleher, J.A., 1972. Rupture zones of large South American earthquakes and some predictions. J. Geophys. Res. 77, 2087. https://doi.org/10.1029/JB077i011p02087.
   Kennett, B.L.N. (Ed.), 1991. IASPEI 1991 Seismological Tables. Bibliotech, Canberra, Australia.
- Kerr, A.C., Aspden, J.A., Tarney, J., Pilatasig, L.F., 2002. The nature and provenance of accreted oceanic terranes in western Ecuador: geochemical and tectonic constraints. Mem. Geol. Soc. Lond. 159, 577–594. https://doi.org/10.1144/0016-764901-151.
- León-Ríos, S., Agurto-Detzel, H., Rietbrock, A., Alvarado, A., Beck, S., Charvis, P., Edwards, B., Font, Y., Garth, T., Hoskins, M., Lynner, C., Meltzer, A., Nocquet, J.M., Regnier, M., Rolandone, F., Ruiz, M., Soto-Cordero, L., 2019. 1D-velocity structure and seismotectonics of the Ecuadorian margin inferred from the 2016 M<sub>w</sub>7.8 Pedernales aftershock sequence. Tectonophysics 767, 228165. https://doi.org/10.1016/j.tecto.2019.228165.
- Manchuel, K., Régnier, M., Béthoux, N., Font, Y., Sallarès, V., Díaz, J., Yepes, H., 2011. New insights on the interseismic active deformation along the North

- Ecuadorian-South Colombian (NESC) margin. Tectonics 30, 1–25. https://doi.org/10.1029/2010TC002757
- Meltzer, A., Beck, S., Ruiz, M., Hoskins, M., Soto-Cordero, L., Stachnik, J.C., Lynner, C., Porritt, R., Portner, D., Alvarado, A., Hernandez, S., Yepes, H., Charvis, P., Font, Y., Regnier, M., Agurto-Detzel, H., Rietbrock, A., Leon-Rios, S., Diego Mercerat, E., 2019. The 2016 M<sub>w</sub> 7.8 pedernales, Ecuador, earthquake: rapid response deployment. Seismol. Res. Lett. XX, 1–9. https://doi.org/10.1785/0220180364.
- Mendoza, C., Dewey, J.W., 1984. Seismicity associated with the great Colombia-Ecuador earthquakes of 1942, 1958 and 1979: implications for barrier models of earthquake rupture. Bull. Seismol. Soc. Am. 74, 577–593. https://doi.org/10. 1785/0120000505.
- Migeon, S., Garibaldi, C., Ratzov, G., Schmidt, S., Collot, J.Y., Zaragosi, S., Texier, L., 2017. Earthquake-triggered deposits in the subduction trench of the North Ecuador/South Colombia margin and their implication for paleoseismology. Mar. Geol. 384, 47–62. https://doi.org/10.1016/j.margeo.2016.09.008.
- Mothes, P.A., Nocquet, J.-M., Jarrín, P., 2013. Continuous GPS network operating throughout Ecuador. Eos 94, 229–231. https://doi.org/10.1029/2012E0090001.
- Nippress, S.E.J., Rietbrock, A., 2007. Seismogenic zone high permeability in the Central Andes inferred from relocations of micro-earthquakes. Earth Planet. Sci. Lett. 263, 235–245. https://doi.org/10.1016/j.epsl.2007.08.032.
- Nocquet, J.-M., Jarrin, P., Vallée, M., Mothes, P.A., Grandin, R., Rolandone, F., Delouis, B., Yepes, H., Font, Y., Fuentes, D., Régnier, M., Laurendeau, A., Cisneros, D., Hernandez, S., Sladen, A., Singaucho, J.-C., Mora, H., Gomez, J., Montes, L., Charvis, P., 2017. Supercycle at the Ecuadorian subduction zone revealed after the 2016 Pedernales earthquake. Nat. Geosci. 1, 1-8. https://doi.org/10.1038/ngeo2864.
- Nocquet, J.-M., Villegas-Lanza, J.C., Chlieh, M., Mothes, P.A., Rolandone, F., Jarrin, P., Cisneros, D., Alvarado, A., Audin, L., Bondoux, F., Martin, X., Font, Y., Régnier, M., Vallée, M., Tran, T., Beauval, C., Maguiña Mendoza, J.M., Martinez, W., Tavera, H., Yepes, H., 2014. Motion of continental slivers and creeping subduction in the northern Andes. Nat. Geosci. 7, 612. https://doi.org/10.1038/ngeo2217.
- Okada, T., Matsuzawa, T., Umino, N., Yoshida, K., Hasegawa, A., Takahashi, H., Yamada, T., Kosuga, M., Takeda, T., Kato, A., Igarashi, T., Obara, K., Sakai, S., Saiga, A., Iidaka, T., Iwasaki, T., Hirata, N., Tsumura, N., Yamanaka, Y., Terakawa, T., Nakamichi, H., Okuda, T., Horikawa, S., Katao, H., Miura, T., Kubo, A., Matsushima, T., Goto, K., Miyamachi, H., 2015. Hypocenter migration and crustal seismic velocity distribution observed for the inland earthquake swarms induced by the 2011 Tohoku-Oki earthquake in NE Japan: implications for crustal fluid distribution and crustal permeability. Geofluids 15, 293–309. https://doi.org/10.1111/gfl.12112.
- Poli, P., Jeria, A.M., Ruiz, S., 2017. The M<sub>w</sub> 8.3 Illapel earthquake (Chile): preseismic and postseismic activity associated with hydrated slab structures. Geology 45, 247–250. https://doi.org/10.1130/G38522.1.
- Reyes, P., 2013. Évolution du Relief Le Long des Marges Actives: Átude de la Déformation Plio-Quaternaire de la Cordillere Cotiere D'Équateur.

- Rolandone, F., Nocquet, J., Mothes, P.A., Jarrin, P., Vallée, M., Cubas, N., Hernandez, S., Plain, M., Vaca, S., Font, Y., 2018. Areas prone to slow slip events impede earth-quake rupture propagation and promote afterslip. Sci. Adv. Geophys. 8, 2–10.
- Segovia, M., Font, Y., Régnier, M., Charvis, P., Galve, A., Nocquet, J.M., Jarrín, P., Hello, Y., Ruiz, M., Pazmiño, A., 2018. Seismicity distribution near a subducting seamount in the Central Ecuadorian subduction zone, space-time relation to a slow-slip event. Tectonics 37, 2106–2123. https://doi.org/10.1029/ 2017TC004771.
- Sokos, E., Zahradnik, J., 2013. Evaluating centroid-moment-tensor uncertainty in the new version of ISOLA software. Seismol. Res. Lett. 84, 656–665. https://doi.org/ 10.1785/0220130002.
- Soto-Cordero, L., Meltzer, A., Bergman, E., Hoskins, M., Stachnik, J.C., Agurto-Detzel, H., Alvarado, A., Beck, S., Benz, H., Charvis, P., Font, Y., Hayes, G., Hernandez, S., Leon-Rios, S., Lynner, C., Nocquet, J.-M., Regnier, M., Rietbrock, A., Rolandone, F., Ruiz, M., 2020. Structural control on megathrust rupture and slip behavior: insights from the 2016 M<sub>w</sub> 7.8 Pedernales Ecuador earthquake. J. Geophys. Res. 125, 1–25. https://doi.org/10.1029/2019/B018001.
- Swenson, J.L., Beck, S.L., 1996. Historical 1942 Ecuador and 1942 Peru subduction earthquakes, and earthquake cycles along Colombia-Ecuador and Peru subduction segments. Pure Appl. Geophys. 146, 67–101. https://doi.org/10.1007/ RE00876670
- Theunissen, T., Font, Y., Lallemand, S., Gautier, S., 2012. Improvements of the maximum intersection method for 3D absolute earthquake locations. Bull. Seismol. Soc. Am. 102, 1764–1785. https://doi.org/10.1785/0120100311.
- Vaca, S., Vallée, M., Nocquet, J.-M., Battaglia, J., Régnier, M., 2018. Recurrent slow slip events as a barrier to the northward rupture propagation of the 2016 Pedernales earthquake (Central Ecuador). Tectonophysics 724–725, 80–92. https://doi.org/ 10.1016/j.tecto.2017.12.012.
- Vallée, M., Nocquet, J.M., Battaglia, J., Font, Y., Segovia, M., Régnier, M., Mothes, P., Jarrin, P., Cisneros, D., Vaca, S., Yepes, H., Martin, X., Béthoux, N., Chlieh, M., 2013. Intense interface seismicity triggered by a shallow slow slip event in the Central Ecuador subduction zone. J. Geophys. Res., Solid Earth 118, 2965–2981. https://doi.org/10.1002/jgrb.50216.
- Wang, R., Martín, F.L., Roth, F., 2003. Computation of deformation induced by earth-quakes in a multi-layered elastic crust FORTRAN programs EDGRN/EDCMP. Comput. Geosci. 29, 195–207. https://doi.org/10.1016/S0098-3004(02)00111-5.
- Wells, D.L., Coppersmith, K.J., 1994. New empirical relationships among magnitude, rupture length, rupture width, rupture area, and surface displacement. Bull. Seismol. Soc. Am. 84. 974–1002.
- Ye, L., Kanamori, H., Avouac, J.P., Li, L., Cheung, K.F., Lay, T., 2016. The 16 April 2016, MW 7.8 (MS 7.5) Ecuador earthquake: a quasi-repeat of the 1942 MS 7.5 earthquake and partial re-rupture of the 1906 MS 8.6 Colombia–Ecuador earthquake. Earth Planet. Sci. Lett. 454, 248–258. https://doi.org/10.1016/j.epsl.2016.09.006.